Direct evidence of overdamped Peierls-coupled modes in the temperature-induced phase transition in tetrathiafulvalene-chloranil

A. Girlando,[1] M. Masino,[1] A. Painelli,[1] N. Drichko,[2,3] M. Dressel,[2] A. Brillante,[4] R. G. Della Valle,[4] and E. Venuti[4]
[1]*Dipartimento di Chimica Generale ed Inorganica, Chimica Analitica e Chimica Fisica, and INSTM-UdR Parma, Università di Parma, Parco Area delle Scienze, 43100-I Parma, Italy*
[2]*1. Physikalisches Institut, Universität Stuttgart, Pfaffenwaldring 57, 70550 Stuttgart, Germany*
[3]*Ioffe Physico-Technical Institute Russian Academy of Sciences, Politeknicheskaya 26, 194021 St. Petersburg, Russia*
[4]*Dipartimento di Chimica Fisica e Inorganica and INSTM-UdR Bologna, Università di Bologna, Viale Risorgimento 4, 40136-I Bologna, Italy*
(Received 21 December 2007; revised manuscript received 5 June 2008; published 3 July 2008)

In this paper, we elucidate the optical response resulting from the interplay of charge distribution (ionicity) and Peierls instability (dimerization) in the neutral-ionic ferroelectric phase transition of tetrathiafulvalene-chloranil, a mixed-stack quasi-one-dimensional charge-transfer crystal. We present far-infrared reflectivity measurements down to 5 cm^{-1} as a function of temperature above the phase transition (300–82 K). The coupling between electrons and lattice phonons in the pretransitional regime is analyzed on the basis of phonon eigenvectors obtained through quasiharmonic lattice dynamics, combined with the results of exact numerical diagonalization of the one-dimensional Peierls-Hubbard model. The resulting multiphonon Peierls coupling leads upon approaching the phase transition to a progressive shift of spectral weight and of the coupling strength toward the phonons at lower frequencies, ending in a soft-mode behavior only for the lowest-frequency phonon near the transition temperature. Moreover, in the proximity of the phase transition, the lowest-frequency phonon becomes overdamped due to anharmonicity induced by its coupling to electrons. The implications of these findings for the neutral-ionic transition mechanism are discussed.

DOI: 10.1103/PhysRevB.78.045103 PACS number(s): 71.30.+h, 71.28.+d, 71.38.−k, 78.30.Jw

I. INTRODUCTION

In a formulation similar to a student's exercise, more than 50 years ago Peierls[1] pointed out that one-dimensional (1D) metals are intrinsically unstable with respect to lattice distortions opening a gap at the Fermi energy. It did not take a long time to realize that the quasi-1D electronic structure of organic charge-transfer (CT) conductors offers an almost ideal model for the Peierls mechanism. Extensive investigations in the 1970s revealed that the Peierls instability may occur also in 1D Mott insulators due to coupling of the lattice to spin (spin Peierls)[2] or to both electronic and spin degrees of freedom ("generalized" Peierls instability).[3] At the time, attention was largely devoted to segregated-stack CT crystals, where identical electron-donor (D) or acceptor (A) π molecules are arranged face-to-face along one direction. Mixed stacking ($\cdots$DADA$\cdots$) received far less attention, at least until a new kind of phase transition was discovered in these systems, the so-called neutral-ionic phase transition (NIT).[4,5] NIT is characterized by a change of ionicity ϱ, i.e., of the amount of charge transferred from D to A in the ground state. Temperature T or pressure p may induce a change from a quasineutral (N, $\varrho \lesssim 0.5$) to a quasi-ionic (I, $\varrho \gtrsim 0.5$) ground state. It was early recognized that the ionic state is subject to the Peierls instability, yielding a stack dimerization ($\cdots$DA DA DA$\cdots$).[6–8]

NIT are complex phenomenas resulting from the competition between two instabilities, the Peierls and the valence (N-I) instabilities, with the corresponding order parameters, the dimerization δ and the ionicity ϱ.[9,10] A specific and interesting feature of mixed-stack CT crystals upon approaching the N-I borderline is the progressive increase in the electronic delocalization along the stack, leading to an amplification of the response of the electronic system to the perturbation from the vibrational degrees of freedom.[11] Mixed-stack CT crystals then offer an almost unique opportunity to study the effects of the increasing electronic susceptibility, hence of the amplified electron-phonon (e-ph) coupling, as the system moves from a weak-coupling regime, far in the N region, toward a strong-coupling regime, when the N-I crossover is approached. Moreover, and at variance with segregated-stack crystals, the Peierls mode is optically active in mixed-stack structures[7] so that it can be detected and characterized by optical methods. Finally, since the dimerized ionic stack is potentially ferroelectric,[12] the Peierls mode is the counterpart of the so-called ferroelectric mode of perovskite-type crystals.[13]

As a consequence of the increase in the electronic susceptibility upon approaching the phase transition, NITs present a rich and intriguing phenomenology, such as the dramatic increase in the dielectric constant or the observation of diffuse x-ray scattering signals.[14,15] These phenomena have been initially ascribed to the occurrence of a new class of collective excitations, the so-called neutral-ionic domain walls (NIDWs).[16] An alternative explanation has been recently proposed in terms of the large charge oscillations induced by the soft dimerization mode upon approaching the N-I crossover.[17–19] It is then of fundamental importance to identify this dimerization or Peierls mode in order to confirm or refute the above suggestion and to shed light on the NIT mechanism.

Direct and clear experimental identification and characterization of the Peierls mode and of its role in the NIT have proved to be more difficult than expected.[20,21] One of the

reasons is that the phonon structure of molecular crystals is very complex so that a reliable understanding of the phonon dynamics is a necessary prerequisite. We have recently undertaken such an analysis for tetrathiafulvalene-chloranil (TTF-CA), the prototypical mixed-stack CT crystal undergoing a first-order temperature-induced NIT at 81 K.[5] In a first paper (hereafter Paper I),[22] we presented quasiharmonic lattice dynamics (QHLD) calculations of TTF-CA lattice phonons above and below the transition temperature and gave a first partial interpretation of the infrared (IR) and Raman spectra. In the present paper, we concentrate on the identification of the Peierls (soft) modes in the TTF-CA *N* phase, searching for the effects of amplified e-ph coupling upon approaching the transition. The corresponding analysis for the *I* dimerized stack phase is deferred to a separate report.[23]

The paper is organized as follows. Sections II and III are devoted to the presentation of the detailed and accurate experimental data for TTF-CA single crystals in the spectral region of 5–200 cm^{-1}, collected in the temperature range down to 82 K. Particular attention is devoted to the submillimeter spectral range, below 30 cm^{-1}. Section IV describes the multimode Peierls coupling model adopted to interpret the spectra. This model combines the information on lattice phonon dynamics reported in Paper I (Ref. 22) with the results from the exact diagonalization of the 1D Peierls-Hubbard Hamiltonian in Ref. 18. In Sec. V we fit the model parameters to the experimental reflectivity spectra to fully account for the data and their temperature dependence. In this way we demonstrate that *mode mixing* and *overdamping* are the key to explain the changes in the far-IR spectra upon approaching the transition. Section IV summarizes the paper's achievements in the broader context of temperature-induced NIT, comparing the present analysis to those based on different interpretative models. The perspectives and limitations of our approach are also discussed.

II. EXPERIMENTAL METHODS

TTF-CA single crystals were grown by sublimation. Crystals as large as 4×4 mm^2 allowed for measurement down to 5 cm^{-1}. The reflectivity was probed on well-developed naturally grown *ab* crystal faces along the optical axes. The crystals were oriented at room temperature according to the known spectra in the mid-IR region using a Hyperion IR microscope attached to Bruker IFS66v Fourier-transform spectrometer. Only spectra polarized along the *a* stack axis are presented as they are the only ones relevant to the analysis of Peierls coupling in the neutral phase.[22] We have indeed verified that reflectivity spectra between 35 and 700 cm^{-1} and polarized perpendicularly to the stack are weak (~10% reflectivity) and do not show significant change from 300 K down to the transition temperature.

The reflectivity spectra were collected by three different setups and techniques, depending on the spectral region of interest: (i) In the 5–30 cm^{-1} region, we employed a quasioptical submillimeter spectrometer, equipped with backward wave oscillator as a coherent and tunable source; a Golay cell served as a detector. Temperature-dependent measurements were conducted in an exchange-gas helium cryostat. The absolute reflectivity was obtained by comparing sample reflectance to reflectance of an aluminum mirror fixed on the same aperture. The spectral resolution in this range is better than 0.01 cm^{-1}. (ii) In the 20–150 cm^{-1} range the reflectivity was measured by a Bruker IFS66v with a spectral resolution of 0.5 cm^{-1}. The spectrometer was equipped with a 1.4 K Si bolometer and a CryoVac cold-finger cryostat. The sample was fixed on the cold finger by carbon paste; a good temperature contact was ensured by Apiezon paste. To get absolute values of reflectivity, the *in situ* gold-evaporation technique was adopted:[24] after measuring the temperature dependence of the sample reflectivity, gold is evaporated onto the sample surface and used as a reference. (iii) Reflectance measurements in the 100–6000 cm^{-1} range were done in a Bruker IFS 113v Fourier transform infrared (FTIR) spectrometer equipped with a 4.2 K Si bolometer, a mercury cadmium telluride (MCT) detector, and an exchange-gas helium cryostat. The absolute reflectivity values of the sample have been obtained by a comparison to a Au mirror of the same size. In this spectral range, a resolution of 2 cm^{-1} was chosen. The reflectivity values agree well with available literature data,[25] which extend from 3000 to 14 000 cm^{-1} and thus cover the charge-transfer transition. The extension to high wave numbers is needed to obtain reliable Kramers-Kronig transformation (KKT) of the data.

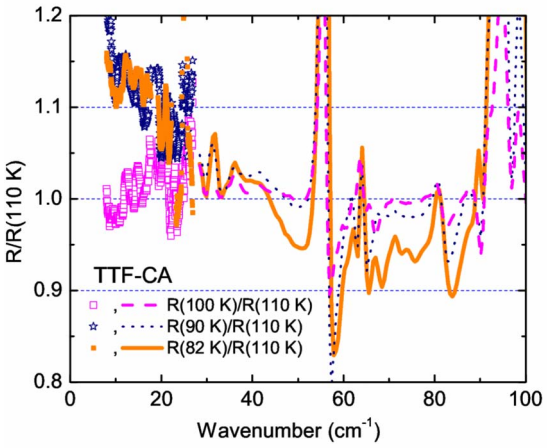

FIG. 1. (Color online) Ratio of the reflectivity spectra at 82, 90, and 100 K to the reflectivity at 110 K. Measurements in the range below 25 cm^{-1} performed by using a submillimeter spectrometer (points) and data above 25 cm^{-1} collected by using a Bruker 66v spectrometer (lines).

We ensured that good overlap exists between the data measured in the three spectral regions. In order to match the absolute values, the submillimeter data were rescaled to those obtained by the Bruker IFS66v FTIR because the *in situ* gold-evaporation technique ensures the most precise measurements of the absolute reflectivity and does not depend on the quality of the sample surface. The quality of the data in the low-frequency region is illustrated in Fig. 1, where the reflectivity at $T=82$, 90, and 100 K is normalized to the reflectivity at 110 K. We see the good overlap between submillimeter and FIR data, collected with two different

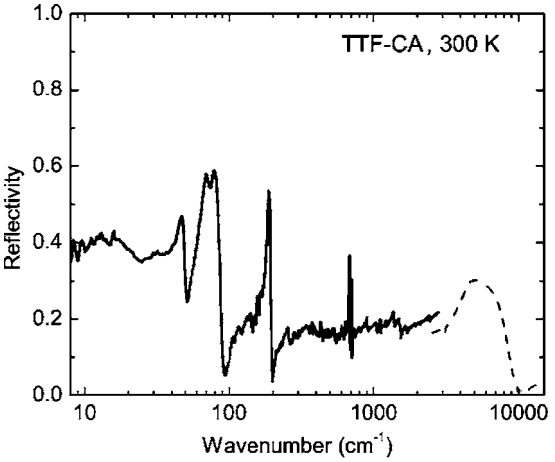

FIG. 2. Experimental reflectivity spectrum of TTF-CA at $T=300$ K with the polarization $E\|a$. The spectral region above 3000 cm^{-1} (dashed curve) is taken from Ref. 25. Notice the logarithmic frequency scale.

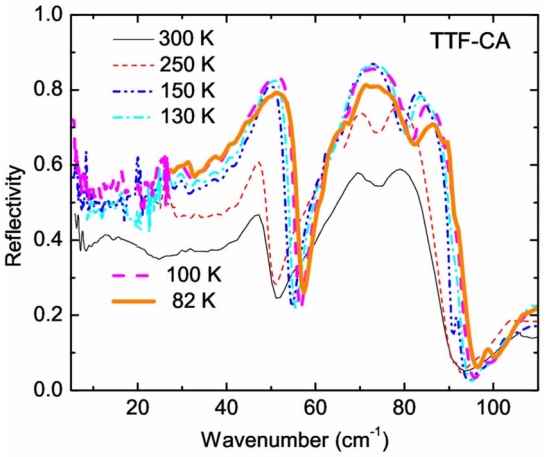

FIG. 3. (Color online) Reflectivity spectra of TTF-CA single crystal along the a axis taken at different temperatures $T>T_c$ above the N-I transition.

instrumentations. The difference of reflectivity ratio $R(T)/R(110\ \mathrm{K})$ for these two spectral regions is indeed smaller than the noise of the measurements.

In the KKT analysis the data were extrapolated below 5 cm^{-1} to fit the known values of the static dielectric constant ϵ_1.[14] We also verified that an extrapolation to a constant value does not significantly affect the conductivity calculated in experimentally accessible region. At frequencies above 14 000 cm^{-1} an extrapolation $R(\omega)\propto\omega^{-2}$ has been used.

III. REFLECTIVITY AND CONDUCTIVITY SPECTRA

Figure 2 shows the room-temperature TTF-CA reflectivity along the stack axis in the experimentally accessible spectral range of 5–6000 cm^{-1} up to 14 000 cm^{-1} taken from Ref. 25. The reflectivity is rather low, as expected for a nonmetallic compound. The charge-transfer electronic transition occurs around 5000 cm^{-1}, and at lower frequencies reflectivity gets down to about 0.2 with no relevant features observed until we encounter the highest-frequency out-of-plane intramolecular modes of CA and TTF at 701 and 682 cm^{-1}, respectively.[26] Below ~250 cm^{-1} we find the bands corresponding to the phonons we want to discuss in the present paper.

The temperature dependence of the reflectivity spectra between 5 and 120 cm^{-1} is presented in Fig. 3. We report only this spectral range since on cooling the sample from 300 to 82 K, the reflectivity above 120 cm^{-1} reveals only unimportant changes. Instead Fig. 3 shows that dramatic changes occur below 100 cm^{-1} with the reflectivity rising by 1.5 times on lowering temperature to 82 K just before the NIT. As discussed in Paper I,[22] below the transition temperature ($T_c=81$ K) the reflectivity drops down to values below those measured at $T=300$ K and barely changes upon further cooling down to 10 K.

A more detailed inspection of Fig. 3 provides evidence that the strongest increase in reflectivity, from about 0.4 to 0.6, occurs on cooling between 300 and 150 K. A further increase in reflectivity below approximately 40 cm^{-1} is observed upon approaching the phase transition, as also evidenced in Fig. 1 above. By lowering T below 100 K, the reflectivity indeed drops in the range of 30–100 cm^{-1} and increases below, indicating a redistribution of the overall spectral weight.

Frequency-dependent conductivity spectra, obtained by the KKT of the reflectivity, are presented in Fig. 4 for several temperatures. As exemplified in Fig. 5 for the two extreme temperatures (300 and 82 K), the conductivity spectra are well reproduced as a sum of several Lorentzian peaks. Specifically, in the region below 100 cm^{-1} six Lorentzian peaks are clearly identified. We label them ν_1 to ν_6 in the order of increasing frequency, as shown in Fig. 5. The temperature evolution of the ν_1 to ν_6 peak frequencies is reported in Fig. 6. In the group of bands with a broad maximum around ~70 cm^{-1} at $T=300$ K, three modes (ν_6, ν_5, and ν_4) are resolved at lower temperatures. While the highest-frequency band, ν_6, shows normal hardening on lowering T, ν_5 and ν_4 frequencies barely move. The ν_3 band at 47 cm^{-1} shows

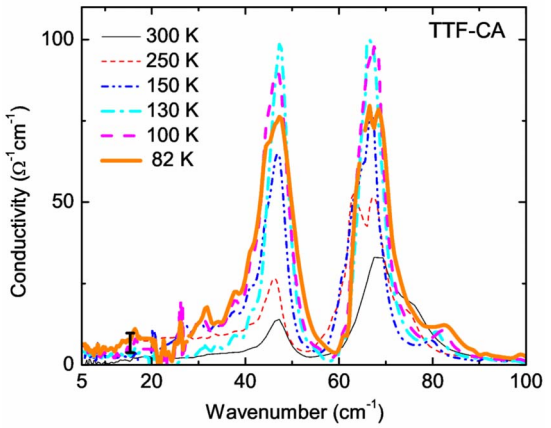

FIG. 4. (Color online) Conductivity spectra along the a stack axis at temperatures above the N-I transition. An error bar for the absolute values of low-frequency conductivity is shown.

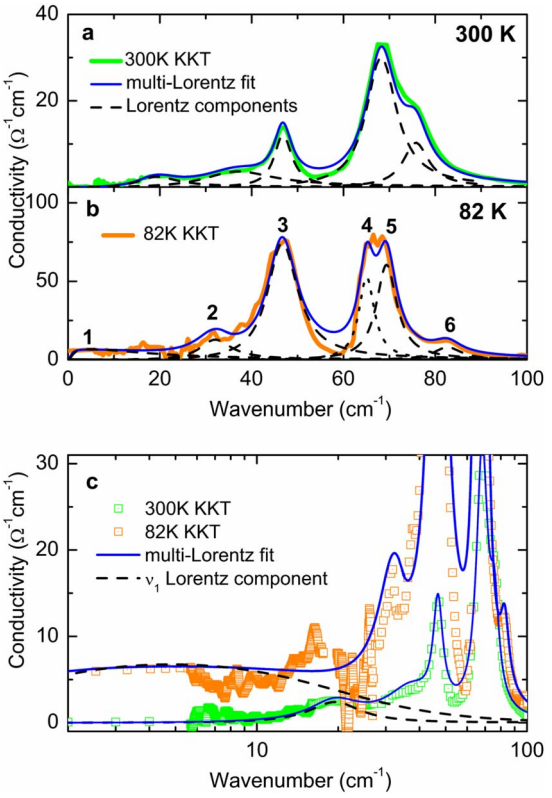

FIG. 5. (Color online) Upper panel: Comparison of the TTF-CA KKT conductivity at 300 K (green line) and 82 K (orange line) with the fit of reflectivity spectra by a minimum number of harmonic oscillators. The Lorentzian bands used in the deconvolution are shown as dashed lines and the resulting conductivity as blue lines. Bottom panel: Comparison of the KKT conductivity with the multi-Lorentzian fit at two different temperatures. The Lorentz component of the lowest-frequency phonon (ν_1) is also shown. Notice the wave-number logarithmic scale.

a very weak softening of ~ 2 cm^{-1} below $T=130$ K. The deconvolution of the low-frequency region of the room-temperature spectrum suggests the presence of bands around 38 and 17 cm^{-1} (ν_2 and ν_1), "appended" to the 47 cm^{-1} band. When going from ambient T to 200 K, the ν_1 band shifts

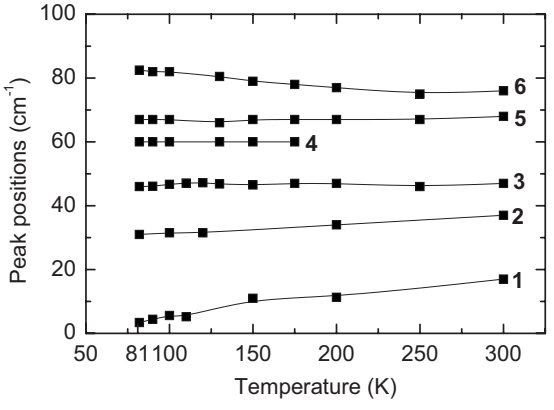

FIG. 6. Temperature dependence of the frequencies of the six phonons bands observed below 100 cm^{-1}, labeled ν_1 to ν_6 going from the lowest to the highest frequency.

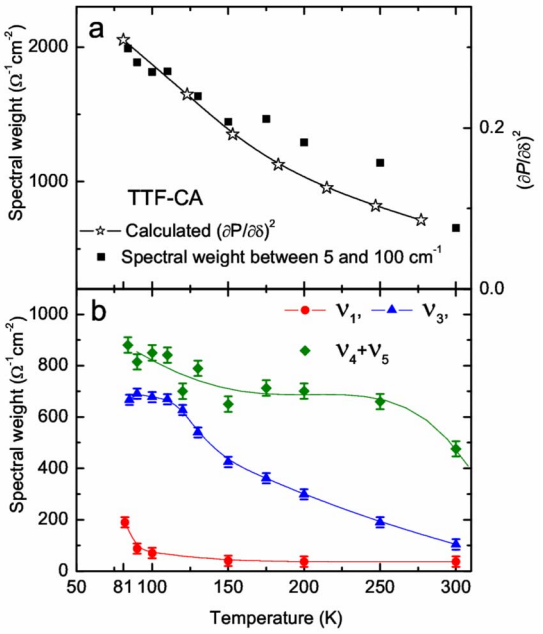

FIG. 7. (Color online) (a) Temperature dependence of the spectral weight of the 0–100 cm^{-1} spectral region (squares) compared with the temperature dependence of $(\partial P/\partial \delta)^2$ (open stars) (Sec. IV). (b) Temperature dependence of the spectral weight of the group of bands around 70 cm^{-1} (ν_4 and ν_5) (rhombs) and of the ν_3 (triangles) and ν_1 (circles) bands. The lines are a guide to the eye.

below 15 cm^{-1} and broadens. Both effects are magnified with a further decrease in T with the frequency dropping down to ~ 5 cm^{-1} at 90 K (Fig. 6) and the band shape resembling a broad background at temperatures just above the phase transition (Fig. 5, bottom panel).

Figure 4 presents an important increase in the overall intensity of conductivity spectra with decreasing T. To quantitatively appreciate the phenomenon, Fig. 7(a) shows the temperature evolution of the spectral weight integrated between 0 and 100 cm^{-1}. The intensities of the individual bands, estimated by integrating in the relevant spectral region, are reported in the lower panel [Fig. 7(b)]. From this panel one sees which bands gain intensity by lowering T: the ν_5 and ν_4 bands (estimated as a whole maximum around 70 cm^{-1} since the bands are not well resolved), the ν_3 band at 47 cm^{-1}, and the ν_1 band. The intensity of the latter increases only below 100 K.

While the spectral weight increases on cooling, it also redistributes toward lower-frequency bands. The temperature dependence of intensity around 70 cm^{-1} has smaller slope below 200 K, whereas the spectral weight of ν_3 (47 cm^{-1}) band saturates at temperatures below 130 K. At this temperature the intensity of the ν_1 band starts to rise rapidly. Just above the transition, from 90 to 82 K, the ν_1 band grows at the expense of the ν_3 one.

At low temperatures the ν_3 and ν_1 bands show considerable anharmonicity. While at $T=300$ K the ν_3 band (47 cm^{-1}) can be fitted by a Lorentzian profile, it becomes wider and very asymmetric at temperatures below 250 K as its lower-frequency wing grows on cooling. The temperature dependence of the full width at half maximum (FWHM) of

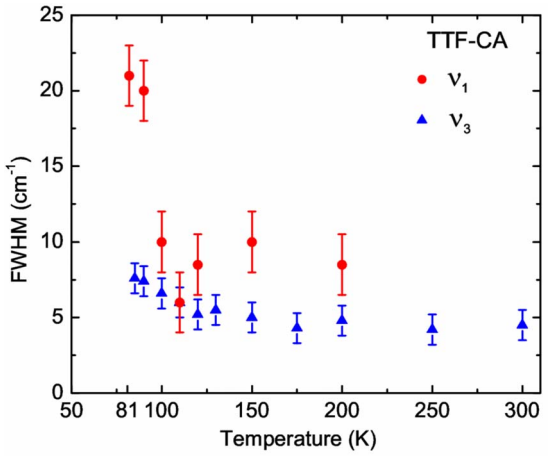

FIG. 8. (Color online) Temperature dependence of the FWHM of the ν_1 (circles) and of the ν_3 (triangles) bands in TTF-CA.

the ν_3 band, directly estimated from experimental spectra (Fig. 5, bottom panel), is displayed in Fig. 8. The same plot shows also the dramatic increase in the FWHM of the lowest-frequency ν_1 band below $T=100$ K with clear *overdamping* at temperatures close to the transition.

The analysis of the spectra points to a very specific behavior of the bands around ~ 70 cm^{-1}, on the one hand, and of the ν_3 and ν_1 bands, on the other hand. Upon lowering T, the bands show a huge intensity increase with a concomitant intensity redistribution between the two groups and important deviations from Lorentzian band shape. Below 100 K, we also observe appreciable softening and large broadening for the lowest-frequency mode. A quantitative explanation of this complex temperature behavior of the spectrum is offered by the model discussed below.

IV. MULTIMODE PEIERLS COUPLING

Electron-phonon coupling is a key issue for understanding the physical and spectral properties of charge-transfer crystals such as TTF-CA.[27] In the framework of a Hubbard-model description of the electronic structure, the e-ph coupling can be separated into two contributions. Molecular vibrations, which preserve the molecular symmetry (i.e., totally symmetric molecular vibrations), couple to CT degrees of freedom through the modulation of on-site energies (electron-molecular vibration or Holstein coupling). Intermolecular or lattice phonons, and possibly out-of-plane molecular vibrations modulate the intermolecular CT integrals (Peierls coupling). The spectral signatures of Holstein coupling show up in mid-IR as well as in Raman spectra of CT crystals and are well understood.[27] The vibrational spectra of TTF-CA in the spectral region relevant to molecular vibrations have been fully analyzed in a series of detailed papers.[11,26,27] Here we focus on Peierls coupling by combining a semiempirical approach for the characterization of the phonon structure with the results of exact numerical diagonalization on the extended Hubbard model for the description of the electronic structure.

The frequencies and normal coordinates of TTF-CA low-frequency phonons at $T=300$ K (N phase) have been calculated by the QHLD method, as described in Paper I.[22] In this calculation we relax the rigid molecule approximation, allowing for the mixing between lattice and low-frequency intramolecular phonons. Therefore *all* phonons with frequency below ~ 250 cm^{-1} enter our calculation, quite irrespective of their (partial) intramolecular or intermolecular nature.

The electronic structure of TTF-CA is described in terms of a modified Hubbard model with adiabatic coupling to zero-wave-vector molecular and lattice vibrations. Specifically, zone-center Peierls phonons enter the Hamiltonian via a modulation of the CT integral alternation, δ. Real space diagonalization of the modified Hubbard Hamiltonian relevant to stacks of up to 18 molecules with periodic boundary conditions yields reliable information on the ground-state properties.[18] It is important to stress that in CT salt electrons are delocalized in one dimension, while both phonons and electrostatic interactions are truly three dimensional. However, three-dimensional electrostatic interactions collapse in the mean-field approximation into an effective 1D model.[7,28] The strong anisotropy of the electronic structure of TTF-CA naturally yields to a Peierls mechanism for the stack dimerization, then justifying the restriction of the e-ph problem to a 1D system. Indeed, far-IR spectra with polarization perpendicular to the stack do not show significant variation on approaching T_c (cf. Sec. II). Interstack Madelung interactions and other three-dimensional interactions such as hydrogen bonding[29,30] most likely cooperate in inducing the first-order valence instability (N-I transition), which takes over the Peierls instability at T_c.

As discussed in Paper I (Ref. 22) and elsewhere,[20,31] in the N phase of TTF-CA the Peierls-coupled phonons transform as the B_u species in the C_{2h}^5 crystal symmetry and are IR active with polarization along the stack axis. They correspond to the out-of-phase combination of the vibrational modes along the two stacks inside the TTF-CA unit cell. We shall therefore restrict our attention to these phonons, whose frequencies, calculated by the QHLD method for the equilibrium structure at 300 K, are reported in the second column of Table I. The atom-atom internuclear potential adopted in the QHLD calculation does not include the CT interaction so that values in Table I are the zero-order reference frequencies in the absence of Peierls coupling. In other words, they correspond to a hypothetical state where the electronic excitations are moved to infinite energy.[27] As a consequence, the frequencies of Table I cannot be directly compared with the experimental frequencies.

The modes with B_u symmetry listed in Table I modulate the CT integral, the corresponding coupling constants being defined as

$$g_i = \sqrt{\frac{\hbar}{2\omega_i}}\left(\frac{\partial t_{\mathrm{DA}}}{\partial Q_i}\right)_{eq}, \tag{1}$$

where t_{DA} is the CT integral between adjacent DA molecules along the stack, and Q_i is the normal coordinate for the ith phonon with frequency ω_i and wave vector $\mathbf{q}=0$. The CT integral and its variation with Q_i have been calculated by the extended Hückel method, adopting the Wolfsberg and Helmholtz approximations.[32] The equilibrium value for the CT

TABLE I. Calculated low-frequency B_u phonons of TTF-CA in the N phase. ω_i, g_i, and ε_i denote the zero-order frequency, Peierls coupling constant, and coupling strength, respectively.

	Mode	ω_i (cm^{-1})	g_i (meV)	ε_i (meV)
B_u	ν_1	27.6	−5.2	7.8
	ν_2	38.6	8.3	14.4
	ν_3	55.8	−8.7	10.9
	ν_4	80.5	−2.2	0.5
	ν_5	90.5	−9.7	8.3
	ν_6	99.4	−17.0	23.4
	ν_7	113.2	−2.3	0.4
	ν_8	118.5	−20.7	29.2
	ν_9	134.0	0.1	0.0
	ν_{10}	194.3	7.9	2.6
	ν_{11}	206.0	−2.4	0.2
	ν_{12}	211.3	−2.9	0.3
	ν_{13}	250.7	−13.8	6.1

integral calculated for the room-temperature geometry is t =0.20 eV, in agreement with current estimates.[18] The g_i values, obtained by numerical differentiation, are listed in the third column of Table I. A useful auxiliary parameter to measure the strength of the Peierls coupling is the relaxation energy for each phonon, $\varepsilon_i=(g_i^2/\omega_i)$, that can be summed up over all phonons to measure the total relaxation energy, ε_d $=\Sigma_i\varepsilon_i$. Our estimate $\varepsilon_d=0.1$ eV is again in reasonable agreement with current estimates.[18] Phonons above 250 cm^{-1} give negligible contribution to ε_d. As a consequence, they are not reported in the table or discussed here.

Both experimental data and the coupling constants in Table I suggest that several modes are appreciably coupled to CT degrees of freedom, leading to a typical *multimode* coupling problem. Due to their common interactions with delocalized electrons, the different vibrations are mixed together, as most clearly demonstrated by the following force-constant matrix, written in the basis of the reference coordinates Q_i,[33]

$$F_{ij}(T) = \omega_i\omega_j\delta_{ij} - \sqrt{\omega_i\omega_j}g_ig_j\chi_b. \quad (2)$$

Here, ω_i and g_i are the reference frequencies and coupling constants of Table I, and χ_b is the electronic response to the phonon perturbation. As usual, the eigenvalues of the force-constant matrix yield the squared vibrational frequencies of the coupled problem, Ω_j^2, while the eigenvectors are the relevant normal coordinates $\mathcal{Q}_j$. The structure of the force-constant matrix in Eq. (2) clearly points to a softening of coupled modes with effects that increase with the electronic susceptibility. Similarly, the absolute values of the off-diagonal elements of the force-constant matrix, responsible for the e-ph induced mixing of vibrational modes, also increase with χ_b: The description of the normal modes varies with the strength of e-ph coupling in a multimode system.

The electronic susceptibility, χ_b, entering Eq. (2), is proportional to the second derivative of the ground-state energy on the dimerization amplitude, δ, and has been calculated in Ref. 18 by exact diagonalization of a modified Hubbard model with parameters optimized to mimic the behavior of TTF-CA. Since from 300 to 82 K the ionicity ϱ changes from about 0.2 to 0.3,[26,34] in the first column of Table II we list the χ_b values corresponding to the ϱ calculated in this interval. By matching the calculated ionicities in the third column of the table with the experimental values,[34] we can translate the ϱ dependence of the calculated χ_b in a T dependence, as reported in the fourth column of Table II.

TABLE II. Calculated electronic response χ_b and squared polarizability derivative $(\partial P/\partial\delta)$ for different degrees of ionicity ϱ. The correspondence between ϱ and T is derived from experiment (Ref. 34).

χ_b (eV^{-1})	$(\partial P/\partial\delta)^2$	ϱ	T (K)
5.797	0.086	0.197	277
6.123	0.103	0.209	247
6.486	0.126	0.222	215
6.894	0.154	0.236	183
7.356	0.192	0.250	153
7.884	0.242	0.266	123
8.493	0.309	0.282	81

The diagonalization of the force-constant matrix in Eq. (2) with the vibrational parameters in Table I and the T-dependent χ_b in Table II leads to the T-dependent vibrational frequencies Ω_j, which can be compared with the experimental frequencies. Figure 9 summarizes the calculated temperature dependence of Ω_j below 100 cm^{-1}. There is substantial agreement between the calculated frequencies in Fig. 9 and the experimental ones in Fig. 6. First of all, in both cases six modes appear below 100 cm^{-1}. Moreover, both experimental and calculated frequencies show an appreciable softening only for the lowest-frequency mode and in close proximity of the phase transition. The weak softening calculated for some modes at higher frequency (Fig. 9) is likely to be compensated by a weak hardening of the reference fre-

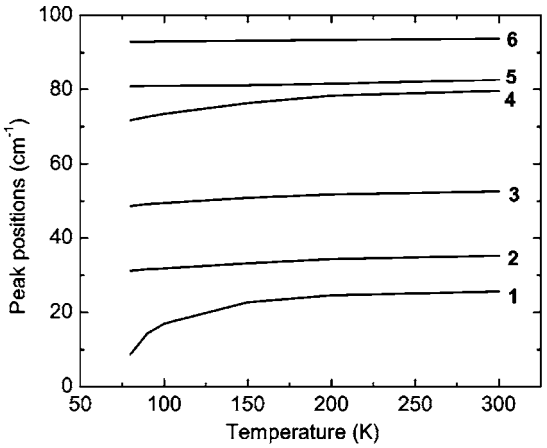

FIG. 9. Temperature dependence of the frequencies of the Peierls-coupled modes, calculated through Eq. (2), using the parameters of Tables I and II.

quencies upon decreasing T, a factor not included in the model, where the reference frequencies are kept T independent.

The multimode calculation quite naturally explains why—although several phonons are coupled to the CT electrons—the observed redshifts of vibrational bands upon approaching NIT is fairly small. The mixing of coupled vibrations [driven by the off-diagonal matrix elements in the force-constant matrix in Eq. (2)], increases with lowering T due to the increase in the electronic susceptibility χ_b. The normal coordinates of the coupled system $\mathcal{Q}_j$ then acquire a T dependence,

$$\mathcal{Q}_j(T) = \sum_i l_{ij}(T) Q_i, \tag{3}$$

where Q_i are the T-independent reference normal coordinate, and $l_{ij}(T)$ are the eigenvectors obtained by diagonalizing the force-constant matrix in Eq. (2) with the T-dependent χ_b in Table II. A T-dependent effective coupling constant can then be assigned to each normal mode of the coupled system,

$$G_j(T) = \sum_i l_{ij}(T) g_i \sqrt{\frac{\omega_i}{\hbar}}. \tag{4}$$

As a result of the χ_b increase upon approaching NIT, the coupling strength, as measured by $[G_j(T)]^2$, progressively transfers from higher- to lower-frequency modes, finally yielding substantial softening of the lowest-frequency phonon.

We now turn our attention to the intensity of vibrational modes. The total intensity of Peierls-coupled modes is proportional to the square of the derivative of the total dipole moment with respect to the dimerization amplitude. Specifically the total oscillator strength induced in a regular mixed stack by the Peierls coupling is[18]

$$f_{\mathrm{P}} = \frac{m_e d^2 \omega_{\mathrm{P}}^2 \varepsilon_d}{t^2} \left(\frac{\partial P}{\partial \delta} \right)^2, \tag{5}$$

where m_e is the electronic mass, d is the equilibrium distance between D and A molecules, and P is the electronic polarizability (i.e., the total dipole moment per site). Calculations based on the modified Hubbard model demonstrate that, at least for regular stacks, the intensity of lattice modes is largely dominated by the contribution from Peierls coupling.[18] The $(\partial P/\partial \delta)^2$ values calculated for parameters relevant to N TTF-CA are reported in the second column of Table II. A first impressive result is the very good matching between the T dependence of the spectral weight measured below 100 cm^{-1} and the T dependence of $(\partial P/\partial \delta)^2$, as shown in the top panel of Fig. 7.

In the multimode Peierls coupling case, the total oscillator strength is partitioned among the coupled modes. Specifically, each normal coordinate $\mathcal{Q}_j$ modulates the CT integral as described by the T-dependent coupling constants $G_j(T)$ in Eq. (4). Using the usual chain rule, the δ derivative of P in Eq. (5) can be rewritten as a sum of $\mathcal{Q}_j$ derivatives. After some algebra we derive the following expression for the IR oscillator strength of each mode coupled to the electronic degrees of freedom,

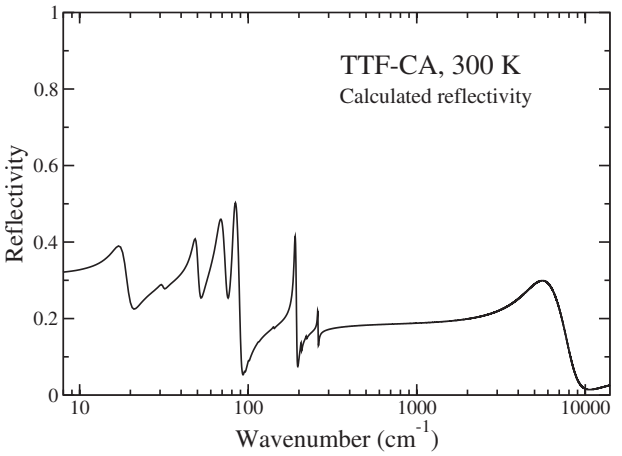

FIG. 10. Calculated reflectivity spectrum of TTF-CA at $T=300$ K with polarization parallel to the stack. Notice the logarithmic frequency scale.

$$f_j(T) = \frac{m_e d^2}{t^2} [G_j(T)]^2 \left(\frac{\partial P}{\partial \delta} \right)^2. \tag{6}$$

Thus the progressive transfer of the coupling strength, $[G_j(T)]^2$, from higher- to lower-frequency modes on lowering T, justifies at the same time the progressive transfer of the softening, as discussed above, and the concomitant transfer of oscillator strength.

Electron-phonon coupling not only affects the vibrational frequencies and intensities but also leads to a broadening of vibrational bands, related to the anharmonicity induced by e-ph coupling. Following Fano,[35] we relate the bandwidth of the Lorentzian line associated with each coupled mode, Γ_j, to the effective strength of the coupling,

$$\Gamma_j(T) = k \frac{[G_j(T)]^2}{\Omega_j} + \Gamma_j^0 = k \eta_j(T) + \Gamma_j^0, \tag{7}$$

where k is an adjustable parameter and Γ_j^0 is the intrinsic vibrational linewidth. Thus the contribution to the damping from e-ph coupling is proportional to $\eta_j = G_j^2/\Omega_j$.

We can now use the standard expression for the frequency-dependent dielectric constant,

$$\epsilon(\omega) = \epsilon_\infty + 8.96857 \cdot 10^{10} \frac{N}{V} \sum_j \frac{f_j}{(\Omega_j^2 - \omega^2) - \mathrm{i}\omega\Gamma_j}, \tag{8}$$

to calculate the contribution of the Peierls-coupled mode to the low-frequency spectra of TTF-CA. The numerical prefactor in Eq. (8) holds for N/V (number of molecules per unit-cell volume) expressed in $\mathrm{Å}^{-3}$ and frequencies and damping in cm^{-1}.

Figure 10 shows the reflectivity spectrum calculated through Eqs. (2)–(4) and (6)–(8). The reference frequencies and coupling constants are taken from Table I. The 300 K values of χ_b and $(\partial P/\partial \delta)^2$, 5.667 eV^{-1} and 0.079, respectively, are obtained from the interpolation of the data in Table II without further adjustment. In addition, we use $d=3.7$ Å, $N/V=4.923\ 86\times 10^{-3}$ $\mathrm{Å}^{-3}$,[31] and $t=0.20$ eV. The CT electronic transition is added in the calculation as an extra term

in Eq. (8), where f_{CT}, Ω_{CT}, and Γ_{CT} are derived directly from experiment.[25] Finally, we set $\epsilon_\infty=2.5$ to account for the high-energy contributions, $\Gamma_j^0=2$ cm^{-1}, for all the modes and $k=0.5$ cm.

The calculated reflectivity in Fig. 10 agrees nicely with the experimental spectrum in Fig. 2, considering that the values of the parameters have been estimated independently from the spectra with the only exceptions of Γ_j^0, k, and the set relevant to the CT and high-energy electronic transitions. The calculated frequencies are well within the usual errors of QHLD calculations (± 10 cm^{-1}). The calculated oscillator strengths for the lower-frequency phonons are just a little below the experiment. The agreement for the oscillator strength of the phonons at higher frequencies is not expected to be precise because high-frequency phonons have intramolecular character and can have a non-negligible "intrinsic" intensity, which is not accounted for in our model.

V. SPECTRAL FITTING

The discussion in Sec. III puts in evidence a quite complex evolution of TTF-CA spectra with temperature, and Sec. IV shows that such behavior is qualitatively reproduced by our model calculation. The softening is important only for the lowest-frequency phonon at temperatures close to T_c. Moreover, an overall increase in reflectivity by lowering T is brought in by the increase in $(\partial P/\partial\delta)^2$, and the shift of spectral weight toward lower frequency is accounted for by the change in the effective coupling constants G_j, as discussed after Eq. (4). However, we can gain a better insight into the factors affecting the temperature evolution of the spectra once a better agreement between experiment and simulation is achieved. To such aim, Table I frequencies and coupling constants are used as starting values for a nonlinear fitting procedure. We choose to fit the reflectivity rather than conductivity spectra, as the former are the genuine experimental data.

Figure 11 illustrates the results of the fit of the reflectivity spectra at three temperatures. The fit is restricted to the spectral region below 150 cm^{-1} so that the CT transition and its variation with temperature[25] are simulated by adjusting ϵ_∞ and the proportionality factor for the damping, k. $\Gamma_j^0=2$ cm^{-1} and g_i of Table I are kept T independent. We allow for minor (few wave numbers) increase in ω_i with lowering T based on the hardening predicted by QHLD calculations for the thermal contraction. As a whole, the quality of the fit is very good: albeit not all the details of the spectrum are precisely reproduced, the essential features are caught. By lowering the temperature, the reflectivity increases with a redistribution of oscillator strengths and bandwidths as the spectral weight shifts toward lower frequencies.

We underline that due to the T dependence of the vibrational frequencies, oscillator strengths, and dampings entering Eq. (8), a standard fit of experimental data would require three adjustable parameters for each vibrational band at each T. To reproduce experimental data below 250 cm^{-1} at three different temperatures, one would then need $3\times13\times3=117$ adjustable parameters, excluding ϵ_∞. In our model instead we account for the T dependence of the spectra on the

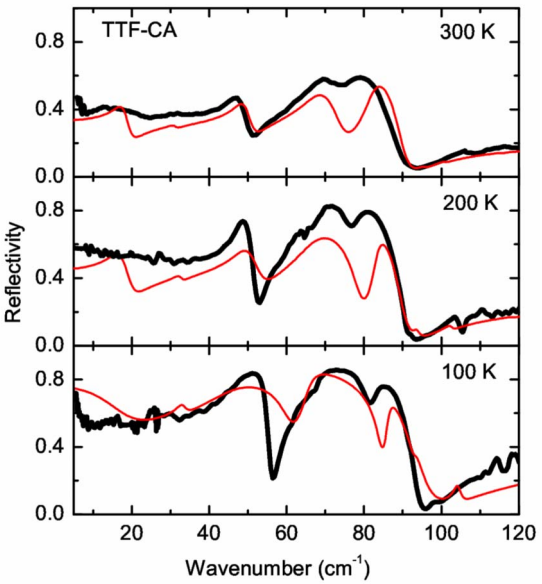

FIG. 11. (Color online) Experimental (thick black line) and calculated (thin red line) low-frequency reflectivity spectra of TTF-CA, parallel polarization, at three different temperatures.

basis of the values of electronic parameters in Table II and by adjusting the reference frequencies ω_i, coupling constants g_i, ϵ_∞, and k. This reduces the number of fitting parameters to $13+13+2=28$ for all temperatures. For this reason, it has been a challenge to obtain the satisfactory reproduction of the spectra shown in Fig. 11.

A better insight into the complex temperature evolution of TTF-CA spectra in the N phase can be obtained from the plot of Fig. 12. In this figure the dotted lines show the temperature dependence of the frequencies of the six Peierls-coupled modes below 100 cm^{-1}, as obtained from the fitting procedure. Overimposed to the frequency curves, we report, for

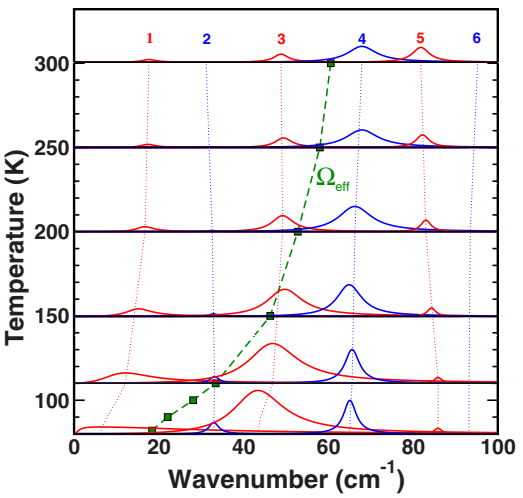

FIG. 12. (Color online) Temperature dependence of the frequency of the six lowest-frequency Peierls-coupled phonons after the fitting to reflectivity spectra. For 300, 250, 200, 150, 110, and 82 K, the calculated individual Lorentzian band shapes are also shown. The green squares connected by a dotted line indicate the frequency of the effective Peierls mode calculated by Eq. (9).

selected temperatures, the calculated single Lorentzians associated with each phonon from ν_1 to ν_6. The analysis is similar to that shown in the top panels of Fig. 5; however, in this case the Lorentzians do not derive from spectral deconvolution but are directly obtained from the conductivity calculated from Eq. (8) on the basis of the fitted parameters.[36]

From Fig. 12 one can appreciate the interplay between the frequency softening, the spectral weight redistribution, and the bandwidth increase. As mentioned in Sec. IV, all the phonons are coupled together through their common interaction with the electronic system [Eq. (2)]. With lowering temperature ϱ increases, leading to a larger electronic delocalization and hence to an amplified χ_b (Table II): Phonons soften as approaching NIT. However, when two phonon frequencies get close they get mixed together and the softening is "transferred" to the lower-frequency phonon. The description of the normal modes evolves with temperature and the coupling strength is progressively transferred to the lower-frequency modes as the phase transition is approached. Indeed all the coupling strength would be eventually transferred to the lowest-frequency ν_1 phonon if the first-order *N-I* instability would not take over before the frequency of this phonon becomes zero.

By lowering T also $(\partial P/\partial\delta)^2$, namely, the spectral weight, increases [Fig. 7(a)]. However, the overall spectral weight is partitioned between the phonons according to Eq. (6), i.e., the individual oscillator strengths are proportional to G_j^2. The partitioning changes with T, and the spectral weight is progressively transferred to the lower-frequency phonons as the phase transition is approached. The shift of the spectral weight is accompanied by an increase in the bandwidth according to Eq. (7). Below 100 K, the coupling strength is almost completely concentrated in the ν_3 and ν_1 phonons, which are both softened. The lowest-frequency phonon has a slightly smaller oscillator strength than ν_3, but its softening is more pronounced. In addition, as the ν_1 frequency moves to very low values, its width increases leading to an overdamping phenomenon. This overdamping reflects the increase in anharmonicity as the dimerization phase transition is approached.

Several independent sets of data collected for TTF-CA, including mid-IR spectra,[34] dielectric measurements,[17,18] or diffuse x-ray scattering data,[19] have been discussed in terms of just one soft Peierls mode. It is therefore important to discuss how this mode is related with the more complex multimode Peierls coupling emerging here from the detailed analysis of TTF-CA far-IR spectra.

The first convincing experimental evidence of the softening of lattice phonons in the TTF-CA *N* phase was obtained some years ago.[34] Several broad bands were found in mid-IR spectra of TTF-CA that could not be assigned to fundamental modes. These bands, whose intensity increases upon approaching NIT, are symmetrically located at the low- and high-frequency sides of a Raman band assigned to a totally symmetric molecular vibration. The two sidebands are then assigned to the sum and difference combinations of the totally symmetric molecular vibration with a lattice phonon. The frequency of this lattice phonon lowers from about 70 cm^{-1} to about 20 cm^{-1} when going from room temperature to 81 K, as illustrated by the dots in the top panel of Fig. 13. In the light of the present work, the soft-phonon inferred from the analysis of combination bands must correspond to an "effective" Peierls phonon, resulting from the weighted contribution of the several Peierls-coupled modes.

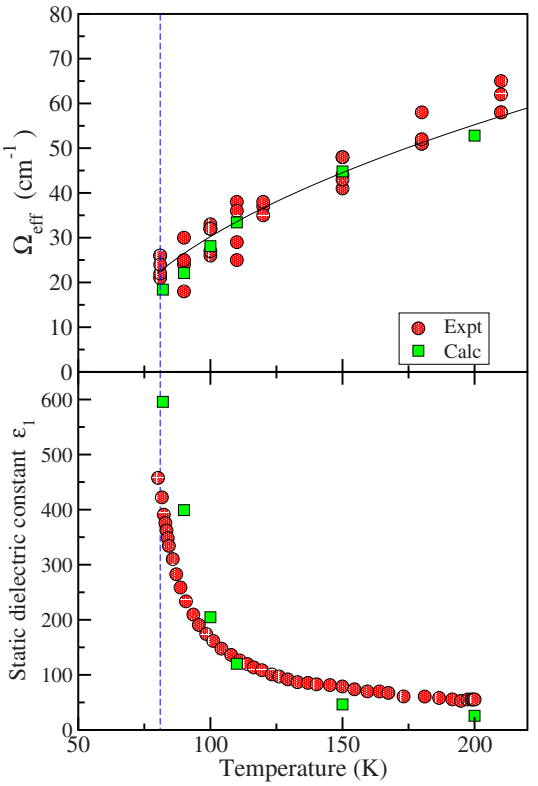

FIG. 13. (Color online) Top panel: Experimental (circles, taken from Ref. 34) and calculated (squares) frequency of the effective soft mode. Bottom panel: Experimental (circles, taken from Ref. 14) and calculated [squares, from Eq. (8)] static dielectric constant of TTF-CA as a function of temperature.

Specifically, the sidebands in the mid-IR region result from the combination of a totally symmetric molecular vibration with a superposition of several B_u modes. Thus the apparent peak frequency of the effective soft mode, Ω_{eff}, is the weighted average of the frequencies of the Peierls phonons. In order to calculate Ω_{eff} from the spectral simulation discussed above, we adopt the following expression:

$$\Omega_{\text{eff}} = \frac{\sum_j \eta_j \Omega_j}{\sum_j \eta_j}, \tag{9}$$

where each frequency is weighted by η_j, the same factor entering the definition of vibrational linewidth in Eq. (7).

The connection of Ω_{eff} with the six lowest-frequency Peierls-coupled modes can be appreciated from Fig. 12, where the frequency obtained from Eq. (9) (green squares connected by a dashed line) is overimposed to the frequencies of the $\nu_1-\nu_6$ phonons. It is seen that Ω_{eff} follows the softening and the shift of spectral weight described by the figure. The comparison of the computed Ω_{eff} with effective frequency obtained from the analysis of combination bands in the mid-IR region is shown in the top panel of Fig. 13.

The agreement between these two totally independent sets of data is impressive and strongly supports our interpretation of the spectroscopic data in terms of a soft mode. Moreover, the same effective soft mode resulting from the analysis of mid-IR data and derived here from the far-IR spectra quantitatively accounts for the temperature evolution of the peaks observed in the diffuse x-ray scattering of the TTF-CA *N* phase.[19]

The softening of the lattice phonons, combined with the increase in their intensity on approaching NIT, leads to very large vibrational contributions to the dielectric constant.[17,18] By using the parameters obtained from the fit of reflectivity spectra, we can also estimate the temperature evolution of the static dielectric constant, ϵ_1, which corresponds to the real part of the zero-frequency dielectric constant along the stack axis, as given by Eq. (8). As shown in the bottom panel of Fig. 13, the present estimate of ϵ_1 agrees very well with available experimental data. This finding strongly supports the vibrational origin of the dielectric anomaly at NIT due to the large charge oscillations along the stack induced by the Peierls mode.[17,18] In directions perpendicular to the stack, the static dielectric constant of our 1D model reduces to ϵ_∞ along that direction, reflecting the experimentally found high anisotropy of the system.[14]

VI. DISCUSSION AND CONCLUSIONS

In this paper, we have presented temperature-dependent polarized reflectivity spectra down to 5 cm^{-1} for TTF-CA crystals in the *N* phase. A very detailed analysis of the experimental data based on a theoretical model that accounts for e-ph coupling in the framework of a modified Hubbard model and relies on QHLD calculation for the definition of the reference normal modes allows us to offer the direct and unambiguous identification of the Peierls softening mechanism in the TTF-CA *N* phase.

Experimental data analogous to the present ones have been previously reported by Okimoto *et al.*,[21] who discussed the reflectivity spectra along the stack of TTF-Q $BrCl_3$ (*Q* $BrCl_3$: 2-bromo-3,5, 6-trichloro-*p*-benzoquinone), a CT crystal similar to TTF-CA that undergoes the NIT with continuous evolution of ionicity. However, in that work the reflectivity data have been collected only from 650 down to 25 cm^{-1} so that the subsequent KKT transformation is delicate, and the discussion of conductivity spectra outside the experimentally accessed region should be taken with caution. In any case, a broad band was enucleated from conductivity spectra which softens, without major broadening, from about 60 cm^{-1} at 293 K to about 10 cm^{-1} just above the critical temperature (71 K). This band was not ascribed to a soft mode rather to the pinned mode of the NIDWs, the neutral-ionic domain walls.[21] Whereas more extensive measurements are required to fully address this issue, our work on TTF-CA sheds doubts on this interpretation.

NIDWs were introduced theoretically by Nagaosa[16] as charged boundaries of *I* dimerized domains excited in the host *N* regular chain. Quite interestingly, they were originally restricted to the close proximity of a discontinuous NIT.[16] NIDWs have been invoked to explain the above-mentioned dielectric anomaly,[14] and the peak in the diffuse x-ray signal,[15] even in regions too far from the NIT to allow for the thermal population of defect states.[37] Indeed, also the combination bands in mid-IR spectra were initially attributed to NIDWs.[38] The present analysis of the temperature evolution of TTF-CA far-IR spectra gives instead very strong support to a different picture, which does not require NIDW excitations. The rich and variegated phenomenology of the NIT can be indeed ascribed to the increase in the electron delocalization and consequent increase in the effective Peierls coupling upon approaching T_c.[18] Different and apparently unrelated experiments are all naturally and *quantitatively* explained in terms of the softening of lattice phonons coupled via a Peierls mechanism to delocalized electrons.[18,19] The only experimental datum not accounted for by the present Peierls model is the abrupt 1 order of magnitude increase of dc conductivity just a few degrees above the TTF-CA NIT.[39] In the temperature region very close to T_c NIDW are likely involved, but their far-IR signatures, if present, cannot be disentangled. On the other hand, NIDWs are accessible at ambient *T* (Ref. 37) and may be important in the *p*-induced NIT of TTF-CA.[40]

The experiment and modeling reported in this paper represent a breakthrough in the optical characterization of Peierls phonons in molecular CT crystals. The analysis presents many analogies with that performed for Peierls-coupled modes in polyacetylene.[41,42] The differences are found in the different models adopted for the electronic structure with the need to resort to strongly correlated models for the NIT and hence to exact diagonalization techniques for the calculation of electronic parameters. The other main difference is in the definition of the reference vibrational problem, which in polyacetylene is obtained by resorting to a well established force field for π-conjugated molecules,[41] whereas here it relies on a more refined QHLD calculation.

In this paper, we have just discussed TTF-CA in the *N* regime. In a forthcoming paper the analysis will be extended to the low-temperature dimerized *I* phase.[23] However, the problem is more difficult since the number of Peierls phonons is greater. In addition, different coupling constants must be introduced to describe the modulation of the two different CT integrals along the dimerized stack.[42] In addition, the spectroscopic effects of e-ph coupling are less prominent than in the *N* phase due to the reduced delocalization of electrons.[22]

The approach illustrated here for TTF-CA can be applied to other *T*-induced NITs in mixed-stack CT crystals, particularly in those crystals where the observation of sidebands in the mid-IR spectra indicates the presence of soft phonons.[9] However, subtle differences may make the analysis more delicate: for instance, in dimethyltetrathiafulvalene-chloranil we observe a continuous or quasicontinuous valence and Peierls instability, but the transition is accompanied by cell doubling, so interstack correlations play a more direct role.[15,43] In any case, the information gained here may be of support also in the interpretation of *p*-induced[4,40] or light-induced NITs,[44,45] which likely occur through a different mechanism.

To summarize, multimode Peierls coupling and overdamping are the key issues to understand the temperature

evolution of the far-IR spectra of TTF-CA in the N regime. The multimode coupling leads to a complex phenomenology driven by the mixing of modes as induced by their coupling to the delocalized electrons. As a result the nature of modes changes with T, and upon approaching the NIT the coupling strength moves from high- to low-frequency modes. Indeed as the system is driven toward the NIT, the Peierls coupling is almost completely transferred to the lowest-frequency mode, whose concomitant broadening leads to an overdamped behavior. For this reason an increase in the reflectivity toward zero frequency is observed close to T_c (Figs. 1 and 3) so that it becomes difficult to actually detect the full band. Overdamping has been often observed in ferroelectric phase transitions.[13] For TTF-CA, we are able to provide the microscopic origin of this effect.

While a multimode coupling model, with its subtleties, is required for a quantitative understanding of far-IR spectra and their temperature evolution, simpler models based on a single effective Peierls mode have been successfully adopted to describe the effects of e-ph coupling on other experimental data.[19,34] The multimode analysis of far-IR spectra presented here offers a quantitative justification for the single mode picture.

ACKNOWLEDGMENTS

The single crystals were kindly supplied by N. Karl (Universität Stuttgart). The work in Italy was supported by the Ministero Istruzione, Università e Ricerca (MIUR) through Grants No. FIRB-RBNE01P4JF and No. PRIN2004033197_002 and in Stuttgart University by the Deutsche Forschungsgemeinschaft (DFG). N.D. thanks the Alexander von Humboldt Foundation and the Scientific Schools under Grant No. NSH-2184.2008.2 for the support.

[1] R. E. Peierls, *Quantum Theory of Solids* (Clarendon, Oxford, 1955), p. 108.
[2] H. M. McConnell and R. J. Lynden-Bell, J. Chem. Phys. **36**, 2393 (1962); D. D. Thomas, H. J. Keller, and H. M. McConnell, *ibid.* **39**, 2321 (1963).
[3] J. W. Bray, L. V. Interrante, I. S. Jacobs, and J. C. Bonner, in *Extended Linear Chain Compounds*, edited by J. S. Miller (Plenum, New York, 1983), Vol. 3.
[4] J. B. Torrance, J. E. Vazquez, J. J. Mayerle, and V. Y. Lee, Phys. Rev. Lett. **46**, 253 (1981).
[5] J. B. Torrance, A. Girlando, J. J. Mayerle, J. I. Crowley, V. Y. Lee, P. Batail, and S. J. LaPlaca, Phys. Rev. Lett. **47**, 1747 (1981).
[6] M. Avignon, C. A. Balseiro, C. R. Proetto, and B. Alascio, Phys. Rev. B **33**, 205 (1986).
[7] A. Girlando and A. Painelli, Phys. Rev. B **34**, 2131 (1986).
[8] N. Nagaosa, J. Phys. Soc. Jpn. **55**, 2754 (1986).
[9] A. Girlando, A. Painelli, S. A. Bewick, and Z. G. Soos, Synth. Met. **141**, 129 (2004).
[10] S. Horiuchi, R. Kumai, Y. Okimoto, and Y. Tokura, Chem. Phys. **325**, 78 (2006).
[11] A. Girlando, R. Bozio, C. Pecile, and J. B. Torrance, Phys. Rev. B **26**, 2306 (1982).
[12] Y. Tokura, S. Koshihara, Y. Iwasa, H. Okamoto, T. Komatsu, T. Koda, N. Iwasawa, and G. Saito, Phys. Rev. Lett. **63**, 2405 (1989).
[13] T. Nakamura, J. Phys. Soc. Jpn. **21**, 491 (1966).
[14] H. Okamoto, T. Mitani, Y. Tokura, S. Koshihara, T. Komatsu, Y. Iwasa, T. Koda, and G. Saito, Phys. Rev. B **43**, 8224 (1991); S. Horiuchi, Y. Okimoto, R. Kumai, and Y. Tokura, J. Phys. Soc. Jpn. **69**, 1302 (2000).
[15] M. Buron-LeCointe, M. H. Lemee-Cailleau, H. Cailleau, S. Ravy, J. F. Berar, S. Rouziere, E. Elkaim, and E. Collet, Phys. Rev. Lett. **96**, 205503 (2006).
[16] N. Nagaosa, J. Phys. Soc. Jpn. **55**, 3488 (1986).
[17] L. Del Freo, A. Painelli, and Z. G. Soos, Phys. Rev. Lett. **89**, 027402 (2002).
[18] Z. G. Soos, S. A. Bewick, A. Peri, and A. Painelli, J. Chem. Phys. **120**, 6712 (2004).
[19] G. D'Avino, A. Girlando, A. Painelli, M. H. Lemée-Cailleau, and Z. G. Soos, Phys. Rev. Lett. **99**, 156407 (2007).
[20] A. Moreac, A. Girard, Y. Dulugeard, and Y. Marqueton, J. Phys.: Condens. Matter **8**, 3553 (1996).
[21] Y. Okimoto, S. Horiuchi, E. Saitoh, R. Kumai, and Y. Tokura, Phys. Rev. Lett. **87**, 187401 (2001).
[22] M. Masino, A. Girlando, A. Brillante, R. G. Della Valle, E. Venuti, N. Drichko, and M. Dressel, Chem. Phys. **325**, 71 (2006).
[23] M. Masino and A. Girlando (unpublished).
[24] C. C. Homes, M. Reedyk, D. A. Cradles, and T. Timusk, Appl. Opt. **32**, 2976 (1993).
[25] C. S. Jacobsen and J. B. Torrance, J. Chem. Phys. **78**, 112 (1983).
[26] A. Girlando, F. Marzola, C. Pecile, and J. B. Torrance, J. Chem. Phys. **79**, 1075 (1983).
[27] A. Painelli and A. Girlando, J. Chem. Phys. **84**, 5655 (1986); C. Pecile, A. Painelli, and A. Girlando, Mol. Cryst. Liq. Cryst. **171**, 69 (1989).
[28] S. Kuwajima and Z. G. Soos, Synth. Met. **19**, 489 (1987).
[29] P. Batail, S. J. LaPlaca, J. J. Mayerle, and J. B. Torrance, J. Am. Chem. Soc. **103**, 951 (1981).
[30] V. Oison, C. Katan, and C. Koenig, J. Phys. Chem. A **105**, 4300 (2001).
[31] M. Le Cointe, M. H. Lemée-Cailleau, H. Cailleau, B. Toudic, L. Toupet, G. Heger, F. Moussa, P. Schweiss, K. H. Kraft, and N. Karl, Phys. Rev. B **51**, 3374 (1995).
[32] A. Landrum and W. V. Glassey, "bind" (Ver. 3.0), distributed as part of the extended Hückel molecular-orbital package (YaHEmop) (http://sourceforge.net/projects/yaehmop/).
[33] A. Painelli and A. Girlando, Phys. Rev. B **37**, 5748 (1988); **39**, 9663 (1989).
[34] M. Masino, A. Girlando, and Z. G. Soos, Chem. Phys. Lett. **369**, 428 (2003).
[35] U. Fano, Phys. Rev. **124**, 1866 (1961).
[36] The fitted values of the frequencies ω_i (at 300 K, in cm^{-1}) and of the coupling constants g_i (in meV) are as follows: ν_1, 20.0 and

−6.5; ν_2, 31.3 and 1.6; ν_3, 51.4 and −6.2; ν_4, 75.5 and −9.0; ν_5, 94.9 and −9.1; and ν_6, 97.4 and −24.3.

[37] Z. G. Soos and A. Painelli, Phys. Rev. B **75**, 155119 (2007).

[38] S. Horiuchi, Y. Okimoto, R. Kumai, and Y. Tokura, J. Phys. Soc. Jpn. **69**, 1302 (2000); J. Am. Chem. Soc. **123**, 665 (2001).

[39] T. Mitani, Y. Kaneko, S. Tanuma, Y. Tokura, T. Koda, and G. Saito, Phys. Rev. B **35**, 427 (1987).

[40] M. Masino, A. Girlando, and A. Brillante, Phys. Rev. B **76**, 064114 (2007).

[41] A. Girlando, A. Painelli, and Z. G. Soos, Chem. Phys. Lett. **198**, 9 (1992); A. Girlando, A. Painelli, and Z. G. Soos, J. Chem. Phys. **98**, 7459 (1993).

[42] A. Girlando, A. Painelli, G. W. Hayden, and Z. G. Soos, Chem. Phys. **184**, 139 (1994).

[43] P. Ranzieri, M. Masino, A. Girlando, and M. H. Lemée-Cailleau, Phys. Rev. B **76**, 134115 (2007).

[44] H. Okamoto, Y. Ishige, S. Tanaka, H. Kishida, S. Iwai, and Y. Tokura, Phys. Rev. B **70**, 165202 (2004).

[45] S. Iwai, Y. Ishige, S. Tanaka, Y. Okimoto, Y. Tokura, and H. Okamoto, Phys. Rev. Lett. **96**, 057403 (2006).